

## RESEARCH ARTICLE

10.1002/2013JC009748

## Special Section:

Pacific-Asian Marginal Seas

## Key Points:

- Seasonal variability of on-shelf intrusion and its causes are examined
- Kuroshio intrusion shows an interannual variation related to ENSO and PDO
- We show major forcing mechanism responsible for nonintrusion events in winter

## Correspondence to:

C.-R. Wu,  
cwu@ntnu.edu.tw

## Citation:

Wu, C.-R., Y.-C. Hsin, T.-L. Chiang, Y.-F. Lin, and I.-F. Tsui (2014), Seasonal and interannual changes of the Kuroshio intrusion onto the East China Sea Shelf, *J. Geophys. Res. Oceans*, 119, 5039–5051, doi:10.1002/2013JC009748.

Received 18 DEC 2013

Accepted 10 JUL 2014

Accepted article online 14 JUL 2014

Published online 12 AUG 2014

## Seasonal and interannual changes of the Kuroshio intrusion onto the East China Sea Shelf

Chau-Ron Wu<sup>1</sup>, Yi-Chia Hsin<sup>2</sup>, Tzu-Ling Chiang<sup>1</sup>, Yong-Fu Lin<sup>1</sup>, and I-Fong Tsui<sup>1</sup><sup>1</sup>Department of Earth Sciences, National Taiwan Normal University, Taipei, Taiwan, <sup>2</sup>Research Center for Environmental Changes, Academia Sinica, Taipei, Taiwan

**Abstract** An advanced artificial neural network classification algorithm is applied to 20 years of multisatellite geostrophic velocity data to study the Kuroshio intrusion onto the southern shelf of the East China Sea. The results suggest that the on-shelf intrusion may occur year round, but winter intrusion events are more frequent than summer events. Both stronger intrusion (which is closely correlated to surface heat flux gradient) and weaker intrusion (which is correlated to wind forcing) occur during wintertime, but the former dominates in late winter while the latter prevails in early winter. There is a significant year-to-year variation of the winter on-shelf intrusion. Although on-shelf intrusion is the major characteristic of the region during wintertime, seldom intrusion events have been identified in the winters of 1997–1998 and 2002–2003. Two conditions are responsible for the cause of the nonintrusion events. During the two nonintrusion winters, the upstream Kuroshio transport anomaly is insignificant (the Kuroshio is not weakened) and no significant winter cooling off northeast Taiwan. Thus, the Kuroshio tends to flow along the shelf break following the 200 m isobath and on-shelf intrusion ceases. Those two nonintrusion events take place during the winters when both the Niño 3.4 index and the PDO index are large and positive.

## 1. Introduction

The Pacific western boundary current, the Kuroshio, flows northward along the eastern coast of Luzon and Taiwan. After leaving Taiwan, the northward-flowing Kuroshio bifurcates when it collides with the zonally running shelf break of the southern East China Sea (ECS) defined by the 200 m isobath [e.g., Hsin *et al.*, 2008]. Figure 1 shows the bathymetry and a schematic sketch of the Kuroshio around the study area. The main stream of the Kuroshio turns eastward following the topography, while a branch intrudes onto the shelf. This on-shelf intrusion branch brings cold subsurface waters to the southern ECS shelf, providing a major source of nutrients to support primary production in the ECS. For example, Chen [1996] demonstrated that the intruded water contributes to a large number of nutrients which are many times more than the deposits from the Yangtze River. Although it is a minor branch of the Kuroshio, the on-shelf intrusion draws much attention because the exchange between the Kuroshio Water and the ECS Shelf Water takes place in the region. The upper-layer Kuroshio on-shelf intrusion is intermittent, and is closely related to the zonal migration of the Kuroshio off the northeastern coast of Taiwan [Wu *et al.*, 2008]. Shoreward deflection of the Kuroshio often induces the on-shelf intrusion. The Kuroshio migration in the area has been observed and investigated using in situ measurements, satellite remote sensing data, high-frequency (HF) radar, and numerical model simulations [e.g., Sun, 1987; Wu *et al.*, 2008; Ichi-kawa *et al.*, 2008; Hsin *et al.*, 2011]. For example, based on 25 year Geomagnetic Electrokinetograph (GEK) measurements, Sun [1987] concluded that the upper-layer Kuroshio migrates seasonally off the northeastern coast of Taiwan, moving shoreward in fall-winter and seaward in spring-summer. A numerical model with refined bathymetry and forcing [Wu *et al.*, 2008] lent support to the finding that the Kuroshio off northeast Taiwan generally shifts seaward (shoreward) in summer (winter). The earlier studies demonstrated that this seasonal change of the Kuroshio was ascribed to the seasonally reversed monsoonal winds (northeasterly in winter and southwesterly in summer) via the Ekman dynamic [Chao, 1991], surface heat flux (SHF) gradient over the ECS shelf via the joint effect of baroclinicity and relief (JEBAR) [Oey *et al.*, 2010], or activities of mesoscale eddies in the Pacific Subtropical Countercurrent (STCC) area [Chang and Oey, 2011]. Nevertheless, Hsin *et al.* [2013] demonstrated that the last cannot be a factor causing the seasonal change of the surface Kuroshio around eastern Taiwan.

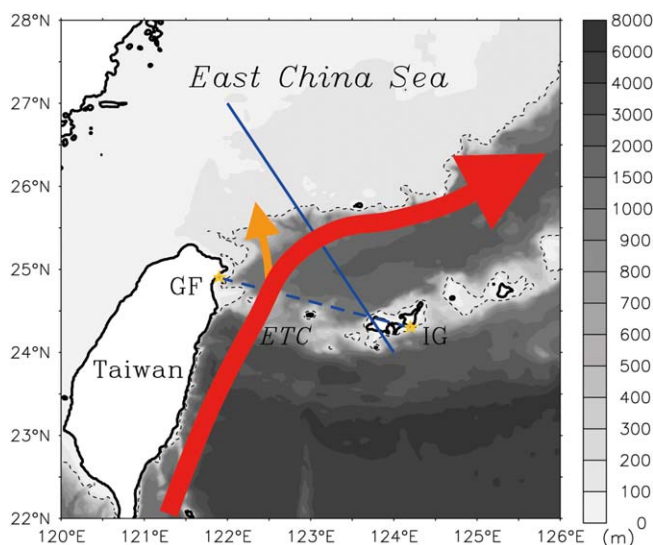


**Figure 1.** Topography and schematic sketches of the Kuroshio (red arrow) and its branch (orange arrow) in the study area. Dashed contour is the 200 m isobath. ETC, GF, and IG are the abbreviations of East Taiwan Channel, Genfang, and Ishigaki, respectively. The two yellow stars on GF and IG denote the positions of two tidal gauges used in this study. Blue line is a cross-shelf section used to validate the variation of surface Kuroshio derived from the satellite-based surface geostrophic velocity. Blue dashed line denotes the section used to calculate the upper-ocean geostrophic transport across the ETC.

Beyond the seasonal time scale, the interannual variability of the Kuroshio migration off northeast Taiwan is seldom explored because long-term measurements are often unavailable in the region. Satellite remote sensing observations have the advantage of continuation and synoptic broad-area coverage. The sea surface temperature (SST) data from satellite can be used in winter to delineate the edge of the Kuroshio by temperature difference, but such data fail during summer when the surrounding SST is usually similar to that of the current. To avoid this disadvantage, we use sea surface height (SSH) from satellite altimeter to perform the present study. In general, ocean dynamics and horizontal

advection in particular play a key part in the interannual variability over the region. SSH instead of SST has been selected because oceanic dynamics is better represented by SSH than SST, which is strongly influenced by the atmosphere (e.g., SHF, evaporation cooling).

Interannual variability in the region was formerly attributed to the El Niño-Southern Oscillation (ENSO) [Hwang and Kao, 2002]. However, especially in the low-latitude western North Pacific, recent studies have noticed that some oceanic phenomena are significantly influenced by the Pacific decadal oscillation (PDO) other than the ENSO in recent years [e.g., Tsui and Wu, 2012; Hsin et al., 2013; Wu, 2013]. In light of these updated findings, the present study also correlates the variations with both the ENSO and the PDO to investigate the possible connection of long-term fluctuations. In addition, by analyzing the SSH-derived surface geostrophic velocity between 1993 and 2012, Hsin et al. [2013] also found that the surface Kuroshio east of Taiwan, the upstream area relative to our study area, varies from year to year. The interannual change of the Kuroshio is highly correlated to the PDO index and is found to be ascribed to the change of relative intensity of cyclonic eddies to anticyclonic eddies off east Taiwan.

Analysis of long-term, continuous satellite remote sensing data for an extensive domain is usually laborious. To address the problem of handling large data sets, synoptic classification is commonly used in statistical (empirical) forecasts. This study proposes the growing hierarchical self-organizing map (GHSOM) classification procedure based on a new advanced artificial neural network classification algorithm to classify satellite remote sensing data into meaningful flow patterns. Since the satellite altimeter-derived geostrophic velocity resolves temporal and spatial scales of interest, we apply the GHSOM to the surface geostrophic velocity to classify dominant patterns of the Kuroshio intrusion onto the southern ECS shelf. To further understand the formation mechanism of the classified flow patterns on seasonal and interannual time scales, the patterns are then correlated with the possible factors (wind forcing, SHF gradient, and the upstream Kuroshio transport) driving the shoreward/seaward movement of the Kuroshio north-east of Taiwan. Besides, according to results of the GHSOM analysis, an intrusion index off northeast Taiwan is defined to investigate the interannual variability of the winter Kuroshio intrusion onto the shelf. We further show the major forcing mechanism responsible for the nonintrusion events in winter. The rest of this paper is structured as follows. Section 2 briefly describes the satellite data and its validation, as well as methodology used in this study. Section 3 shows the main results and discussions. The paper ends with conclusions in section 4.

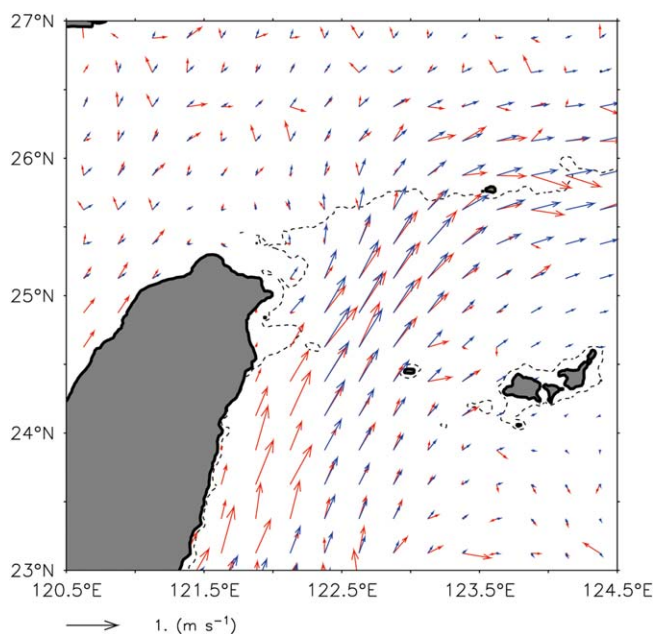


**Figure 2.** Annual mean surface flows around Taiwan. Red arrows denote the mean flow averaged from 20 to 100 m compiled with the Sb-ADCP data from 1991 to 2005 by the National Center for Ocean Research, Taiwan. Blue arrows are the mean surface geostrophic current derived from the altimeter-based sea level anomaly by AVISO. The geostrophic current is interpolated linearly on the same quarter-degree grid as the Sb-ADCP.

## 2. Data and Methodology

### 2.1. Satellite Data and Validations

Because of the extensive accumulation of satellite altimeter data in the recent two decades, surface geostrophic velocities derived from satellite altimeter sea level anomalies of AVISO (Archiving, Validation, and Interpretation of Satellite Oceanographic data) plus mean dynamic topography calculated from altimetry and a geoid model [Rio *et al.*, 2011] were used to investigate the temporal and spatial variation of the upper-ocean flow in the region off northeast Taiwan.

The altimeter data are gridded on a horizontal region of one-third degrees and available from October 1992 to the present with an interval of 1 week.

In this study, we adopt the 20 year data between 1993 and 2012 for analyses. The altimeter-derived surface geostrophic velocity has been widely utilized to explore variations of the Kuroshio east of Taiwan on a broad time scale from a few weeks to several years [Hsin *et al.*, 2010, 2013]. Hsin *et al.* [2010] has carefully validated the altimeter-derived geostrophic velocity with the time series of limited (2000–2001) moored current data off southeast Taiwan. Figure 2 compares the annual mean surface flow from shipboard Acoustic Doppler Current Profiler (ADCP) observations (red arrows) with that of altimeter-based geostrophic velocities (blue arrows). The altimeter-based velocities are comparable to shipboard ADCP velocity composites. This is particularly true in the region around the northeastern coast of Taiwan, including the turning position, magnitude and pathway of the Kuroshio. The on-shelf intrusion of the Kuroshio branch is also well reproduced by this satellite product.

Furthermore, the zonal migration of the surface Kuroshio axis off northeast Taiwan is also seen in altimeter-based geostrophic velocities. Figure 3 shows Hovmöller diagram of the climatological monthly surface geostrophic velocity perpendicular to a cross-shelf section between 27°N, 122°E and 24°N, 124°E (blue line in Figure 1). The white dashed line indicates the intersection of the cross-shelf section and the 200 m isobath. Not only the seasonal Kuroshio migration but also seasonal fluctuations of the Kuroshio intensity are revealed in Figure 3. The Kuroshio intensifies during summertime, reaching its maximum in July (larger than  $0.8 \text{ m s}^{-1}$ ). The western flank of the current is an indicator of the intrusion component. Its location is at  $\sim 122.2^\circ\text{E}$  in January–March, gradually migrating seaward, reaching to its easternmost end at  $\sim 122.7^\circ\text{E}$  in July. Shoreward deflection of the Kuroshio is seen in autumn and migrates westward to  $\sim 122.2^\circ\text{E}$  in December. This seasonality of both the Kuroshio intensity and axial position agrees well with that of surface current derived from HF radars [Ichikawa *et al.*, 2008]. Ichikawa *et al.* [2008] also found that the Kuroshio is stronger in summer, and the faster (slower) Kuroshio velocity accompanies southward (northward) movement of the Kuroshio axis.

To quantify the altimeter-based data further, we compare tidal-gauge-based long-term Kuroshio transports through the East Taiwan Channel (ETC) between Genfang, Taiwan, and Ishigaki, Japan (see Figure 1 for locations) with the altimeter-derived transport through the same section (blue dashed section in Figure 1). The sea level anomaly difference between two tidal stations located at both sides of ETC is used to calculate the Kuroshio transport. The equation to estimate the ETC transport using tidal-gauge measurements is adopted

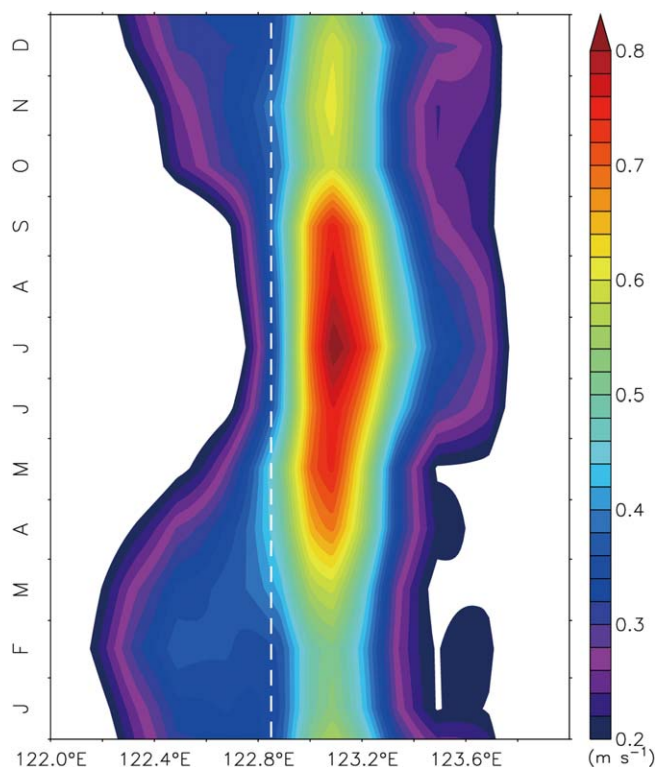


**Figure 3.** Hovmöller diagram of climatological monthly surface Kuroshio derived from altimeter-based geostrophic velocity normal to the blue line shown in Figure 1. White dashed line indicates the intersection of the blue line and the 200 m isobath. Only velocities greater than  $0.2 \text{ m s}^{-1}$  are shown, and those less than  $0.2 \text{ m s}^{-1}$  are filled with white color.

port is estimated from the equation of Yang *et al.* [2001], and then averaged weekly to have the same temporal interval with the satellite altimeter data. As to the altimeter-derived transport, the weekly surface geostrophic velocities are first bilinear-interpolated onto the section between Genfang and Ishigaki. With multiplying a constant depth of 200 m, the cross-section component of geostrophic velocities is then integrated along the section to obtain the transport. When the depth of 200 m is chosen, the altimeter-derived transport has a mean value of about 20 Sv, which agrees well with the mean of the tidal-gauge-derived transport. This result indicates that the 200 m serves as a reference depth for roughly evaluating the Kuroshio transport around Taiwan using the altimeter-derived surface geostrophic current.

Figure 4 shows time series of the Kuroshio transport calculated by altimeter-based data, the tidal-gauge-based transport through the ETC, and the transport derived from the World Ocean Circulation Experiment (WOCE) PCM-1 mooring array [Johns *et al.*, 2001]. The three time series are virtually in phase with each other. Not only the correlation between the altimeter-based and tidal-gauge-based transports is significant at  $\gamma = 0.52$  (the 99% significance level is 0.1), but also the altimeter-based transport correlates closely with the transport derived from the PCM-1 observations ( $\gamma = 0.58$ ). The comparison further demonstrates the reliability of the transport calculation based on altimeter-derived geostrophic velocities. Kuroshio transports are generally smaller during wintertime. However, the annual cycle is not always obvious in the figure because a large intraseasonal signal could hinder identification of the seasonal variability [Hsin *et al.*, 2010, 2013]. The strong intraseasonal fluctuation can be attributed to the interplay between the Kuroshio and mesoscale eddies. In the STCC region ( $20^{\circ}\text{N}$ – $23^{\circ}\text{N}$ ), westward-propagating eddies originating in the interior Pacific frequently approach the eastern coast of Taiwan [e.g., Hwang *et al.*, 2004]. These mesoscale eddies collide with the Kuroshio and influence the flow pattern and volume transport in the downstream region off northeast Taiwan. For example, using altimeter-based SSH anomaly data, Hsin *et al.* [2011] found that the Kuroshio transport variability corresponds closely with the arrival of cyclonic eddies. Hsin *et al.* [2013] further quantified that the intraseasonal fluctuations account for  $>70\%$  of total variance in the Kuroshio east of Taiwan. The cyclonic eddies decelerate the Kuroshio velocity, and hence the Kuroshio shifts shoreward off northeast

from Yang *et al.* [2001]. By regressing the daily sea level anomaly (SLA) difference between Genfang and Ishigaki with the ETC transport ( $Q_{\text{ETC}}$ ) estimated from the World Ocean Circulation Experiment PCM-1 mooring array, Yang *et al.* [2001] suggested a linear relation of  $Q_{\text{ETC}} = 25 \times (\text{SLA}_{\text{Ishigaki}} - \text{SLA}_{\text{Genfang}}) + 20.87$ , where  $Q_{\text{ETC}}$  and SLA are in units of Sv and meter, respectively. Hourly data at Ishigaki, Japan, are obtained from the University of Hawaii Sea Level Center (UHSLC). Those data at Genfang, Taiwan, are provided by the Central Weather Bureau of Taiwan. The ETC transports estimated by tidal-gauge measurements are during the period between February 1994 and May 2008, when the tidal-gauge sea level data at Genfang are available. The hourly tidal-gauge data at both stations are averaged daily in advance.

Afterward, the daily ETC trans-

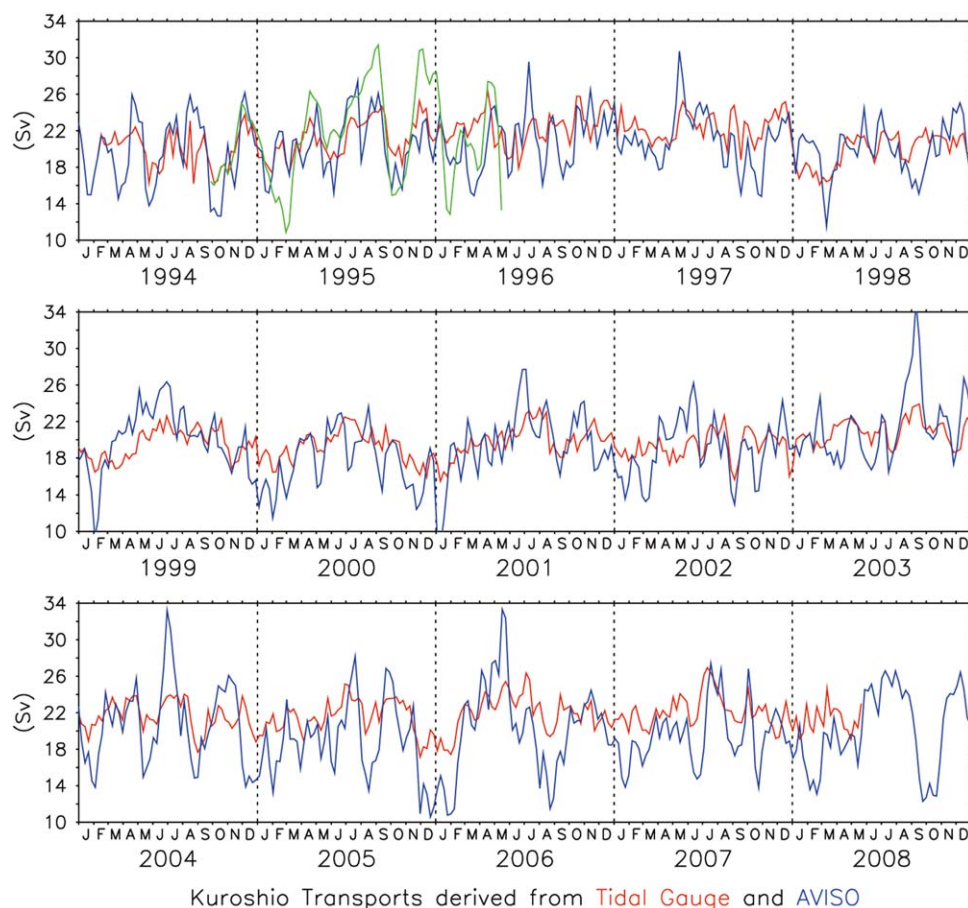


**Figure 4.** Weekly time series of Kuroshio transports through the ETC. Red curve is calculated by the sea level anomaly difference between two tidal gauge stations of Ishigaki and Genfang. Blue curve is derived from the cross-section component of AVISO altimeter-based geostrophic velocity with multiplying a constant depth of 200 m. Green curve is derived from the World Ocean Circulation Experiment (WOCE) PCM-1 mooring array [Johns et al., 2001].

Taiwan. Figure 4 also reveals a significant year-to-year variation. In section 3.3, we will demonstrate that this interannual transport variability is closely related to both the ENSO and the PDO.

Aside from the sea level data, sea surface wind and heat flux are also adopted in this study. Sea surface wind data are based on the Cross-Calibrated Multi-Platform (CCMP) ocean surface wind data sets, which integrate cross-calibrated satellite winds obtained from the Remote Sensing Systems (REMSS) using a Variational Analysis Method (VAM) to produce a high-resolution ( $0.25^\circ$ ) gridded analysis with a temporal interval of 6 h. The CCMP data set is provided by the NASA PO.DAAC (Physical Oceanography Distributed Active Archive Center) and is derived through cross-calibration and assimilation of ocean surface wind data from multiple sensors including microwave radiometers (i.e., SSM/I, SSMIS, AMSR, TMI, and WindSat) and scatterometers (QuikSCAT and SeaWinds). The REMSS uses a cross-calibrated sea surface emissivity model function which improves the consistency between wind speed retrievals from microwave radiometers and those from scatterometers. The CCMP data are available from July 1987 to the end of 2011 and those in the period of 1993–2011 are adopted for the further analyses. SHF data (including sensible heat, latent heat, solar radiation, and long wave radiation) used in this study are obtained from the NCEP/DOE AMIP Reanalysis-2 (National Centers for Environmental Prediction/Department of Energy Atmospheric Model Intercomparison Project Reanalysis-2). The NCEP/DOE AMIP Reanalysis (R-2) is based on the widely used NCEP/NCAR Reanalysis-1 (R-1). The NCEP/DOE AMIP R-2 is an improved version of the NCEP/NCAR R-1 that fixed errors and updated parameterizations of physical processes. The heat flux data have spatial and temporal resolutions of  $2.5^\circ$  and one daily, respectively. The data after 1979 are available and those from 1993 to 2012 are used to compare with the intrusion patterns and index off northeast Taiwan.

## 2.2. Growing Hierarchical Self-Organizing Map (GHSOM)

A self-organizing map (SOM) is an artificial neural network based on unsupervised learning and is an effective software tool for feature extraction [Kohonen, 2001]. The usefulness of the method for this purpose has been demonstrated by several oceanic applications [e.g., Liu and Weisberg, 2005]. Despite its varied applications, SOM analysis has some inherent deficiencies. First, it uses a static network architecture with respect to the number and arrangement of neural nodes that have to be defined before the start of training. Second, hierarchical relationships between the input data are difficult to detect in the map display. To address both of these deficiencies within one framework, the GHSOM was recently introduced. The GHSOM consists of independent SOMs, each of which is allowed to grow in size during the training process until a quality criterion regarding data representation is met. This growth process is continued to develop a layered architecture such that hierarchical relationships between input data are further detailed at lower layers of the neural network.

The GHSOM develops a new architecture that grows both in a horizontal and in a hierarchical way to determine the number of classification patterns and the depth of layers (which control the number of iteration) according to the complexity of the input data. The number of classification patterns and the depth of layers are controlled by the two parameters of "breadth" and "depth," respectively. For the interpretation of oceanographic phenomena, the number of patterns is more meaningful than the depth of layers. In general, the smaller "breadth" is adopted, the more patterns are classified. The greater "depth" is set, the less number of iteration is carried out. This study classifies the patterns derived with breadth = 0.7 and depth = 0.07, which were applied in each iteration until the patterns can be examined by human eyes. In this way, the proposed method both preserves the flexibility of the GHSOM and satisfies the interpretation requirement for the outcome patterns. Additionally, in comparison with the common-used principal component analysis (PCA) or empirical orthogonal function (EOF), which decomposes a complicated data set into several dominant spatial patterns and time series, Liu *et al.* [2006] demonstrated that the GHSOM analysis is more effective in extracting the inherent SST patterns on the western Florida shelf. Their results also showed that the underlying patterns can be visualized in the GHSOM in the same form as the original data while those can only be expressed in the EOF in the form of anomaly. Besides, the GHSOM classifies assertively the map at a time to a single pattern which has the smallest weighted distance from the input data; whereas the EOF analysis occasionally shows a mixture among different modes (patterns).

## 2.3. Kuroshio Intrusion Index

The GHSOM serves as a useful tool for classifying the altimeter-based velocity data to several flow patterns off the northern Taiwan to delineate the behavior of the Kuroshio intrusion onto the ECS shelf. As above mentioned, the GHSOM can classify assertively the original data to the dominant patterns; however, this kind of classification may be somewhat lack of the continuity in describing the evolution of the Kuroshio intrusion. According to the outcome of the GHSOM, we, therefore, define a Kuroshio Intrusion (KI) index off northeast Taiwan to further investigate the temporal evolution of the Kuroshio intrusion onto the ECS shelf. The KI index is calculated by averaging the northward component (i.e.,  $V > 0$ ) of altimeter-derived surface geostrophic current over the region of 25.5°N–26.4°N, 121.9°E–122.5°E. Afterward, by comparing the KI index with the time series of possible factors (wind stress, heat flux gradient, and upstream Kuroshio transport) regulating the Kuroshio intrusion onto the shelf, the relative importance of these factors is clarified.

## 3. Results and Discussion

To study the Kuroshio intrusion onto the ECS shelf, 20 years of gridded mean geostrophic velocities over the area of 24°N–27°N, 121.2°E–123.8°E (the yellow frame in Figure 5) are subjected to the GHSOM analysis for performing the pattern classification. The intrusion criterion is defined as the 0.2 m s<sup>-1</sup> contour of the Kuroshio penetrating through the 200 m isobath. There are two iterations in this study. The GHSOM derives 18 patterns at the first iteration, and 4 patterns at the second. The final classified patterns fall into two categories: intrusion mode and nonintrusion mode. In the SOM each piece of original data are allocated to a particular node (pattern). For each piece of data, a best-matching unit (BMU) is defined by nodes (patterns) that have the smallest weighted distance from the input data and the BMU time series reflects the evolution of these patterns.

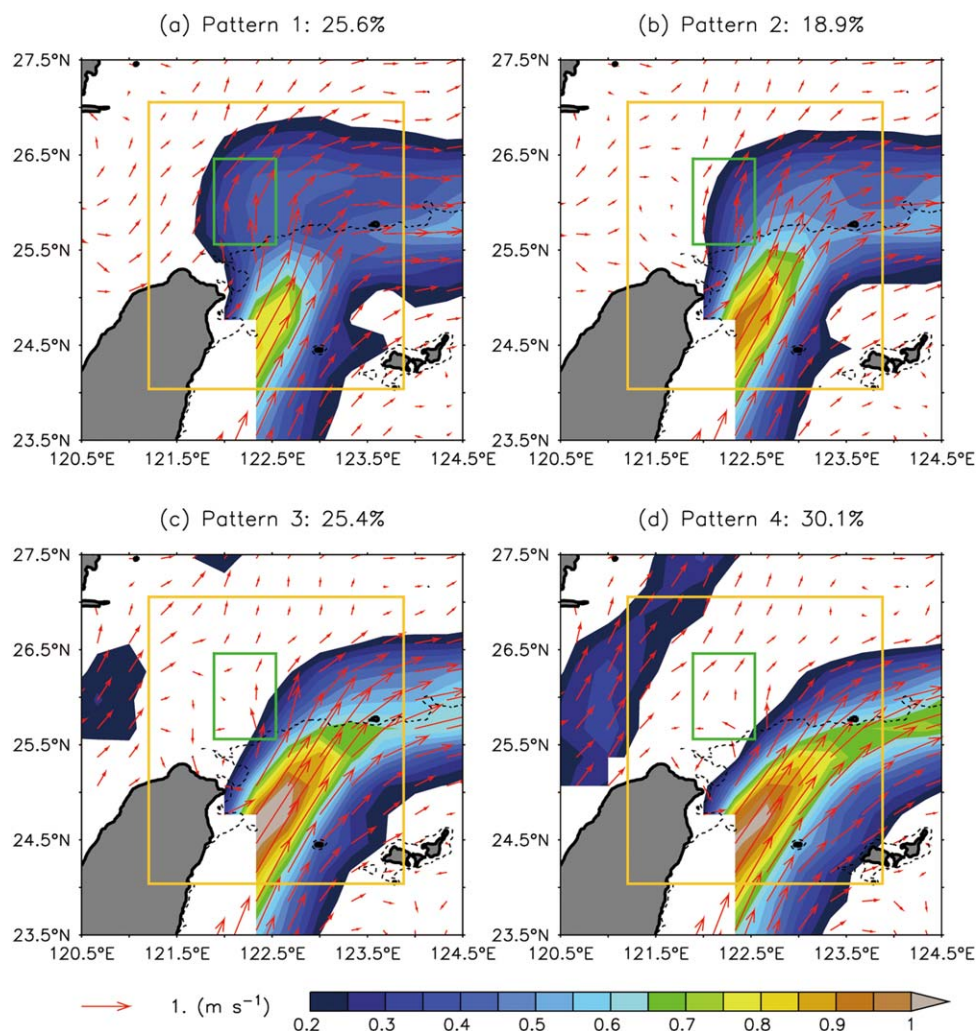


**Figure 5.** GHSOM-derived patterns of the Kuroshio intrusion onto the East China Sea shelf. The occurrence frequency of each pattern is shown at the top of each map. Twenty-year (1993–2012) weekly surface geostrophic velocities in the yellow frame are used for GHSOM to extract the four patterns. Green frame shows the area for calculating the Kuroshio Intrusion (KI) index.

### 3.1. Classified Patterns

Figure 5 shows the four classified patterns. Pattern 1 and pattern 2 belong to intrusion mode, but with different intrusion characteristics. Pattern 1 shows a stronger on-shelf intrusion of the Kuroshio than pattern 2. On the other hand, pattern 3 and pattern 4 are nonintrusion patterns, and both of which show the Kuroshio tends to flow along the shelf break following the 200 m isobath, except for a stronger northward Taiwan Warm Current west of  $\sim 122^{\circ}\text{E}$  in pattern 4. Figure 5 also indicates the occurrence frequency of each pattern. The nonintrusion mode (pattern 3 or pattern 4) appears about 25–30% of the time. The strong intrusion mode (pattern 1) occurs 26% of the time, while the weak intrusion mode (pattern 2) is about 19% of the time. In Figure 6, the weekly BMU shows the temporal evolution of each pattern in the analysis period of 1993–2012. It seems that four patterns prevail in different seasons. Besides, they also possess year-to-year variations. In the later sections, we will describe and discuss the variations on the seasonal and interannual time scales in more detail by further analyses.

### 3.2. Seasonal Variations

To better illustrate the monthly variability, the percentage of BMU of the four patterns, which represents the rate of occurrence of the four patterns, was calculated in Figure 7. Pattern 1 prevails the winter-like months from December to March, while pattern 4 dominates in summer, June through August, with a peak in July. There are two peaks of occurrence in pattern 2, from March to April and from September to

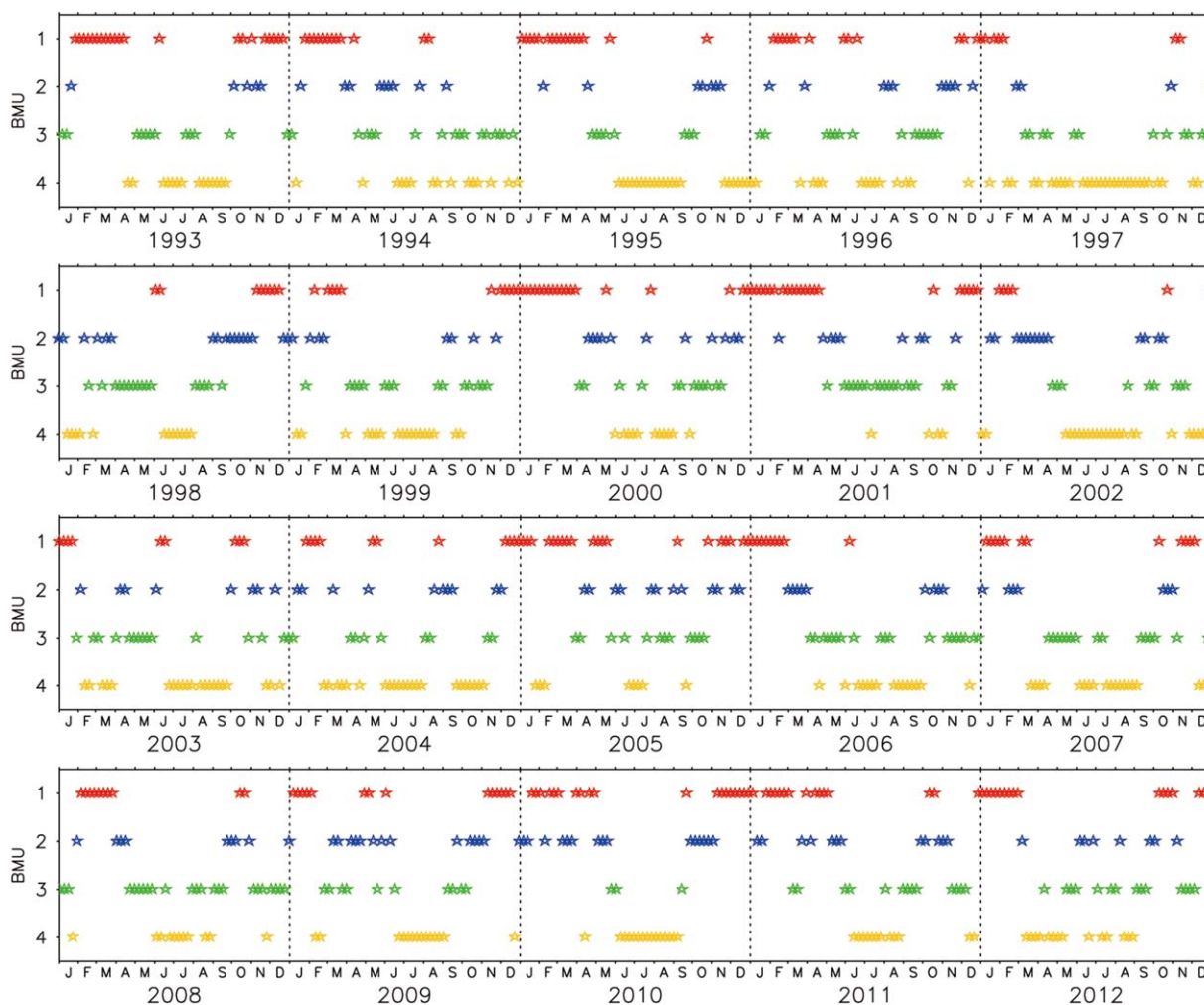
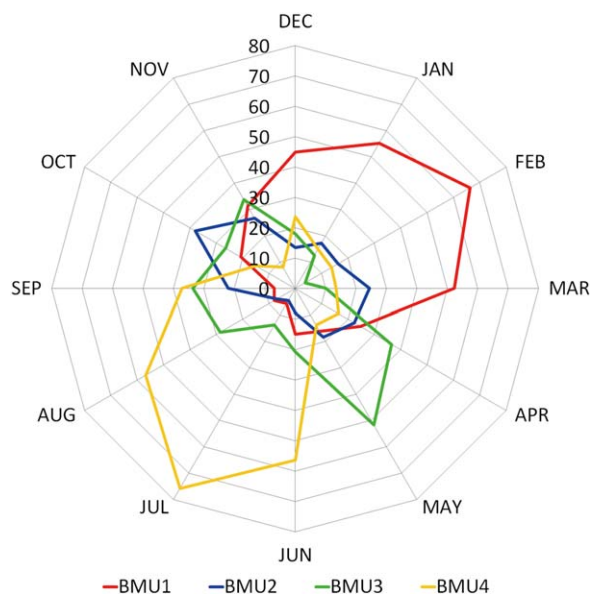


Figure 6. Weekly BMUs of the four patterns of GHSOM.

November, respectively. Pattern 3 also displays two peaks, but in April-May and in August-November. In brief, the two patterns of 2 and 3 take place more frequently in the transition months of summer and winter monsoons; however, pattern 2 occurs more dominantly in months when the winds translate from the summer monsoon into the winter monsoon, whereas pattern 3 prevails in months when the winds translate from the winter monsoon into the summer monsoon. Obviously, each pattern prevails in different months.

The on-shelf intrusion reveals a specific seasonal sequence between these patterns. Following the onset of the southwest monsoon in July (Figure 8), the winter regime gradually enters the summer circulation pattern which is resembled by pattern 4 (Figure 5d). Since both summer monsoon and pressure gradient force in the Taiwan Strait are northward, the northward current originated from the Taiwan Strait is quite strong in summer. The Kuroshio flows northward along the eastern coast of Taiwan, turning eastward off northeast Taiwan, roughly following the continental slope around the 200 m isobath to the northeast. This circulation pattern corresponds with various observations [e.g., *Lie and Cho, 2002; Liang et al., 2003*]. Pattern 2 dominates in the transition months, when the winds are weakened and reversed between summer and winter monsoons. As shown in Figure 8, October marks the beginning of the northeasterly monsoon, which is also the peak appearance of pattern 2 (Figure 7). Afterward, pattern 1 dominates from December to March of the following year as the prevailing northeasterly monsoon strengthens. Pattern 3 rebounds from April to May when the reversal of monsoonal winds takes place. The transition months with weakened wind are again represented by pattern 3. As summer approaches, pattern 4 reaches its maximum in July (~75%), completing the annual cycle.



**Figure 7.** Radar chart of climatological monthly percentages of BMUs of the four patterns derived by GHSOM. Percentage of each pattern in a month is calculated by dividing the number of each pattern by the sum of the four patterns in each month.

Figure 7 also shows that the prominent Kuroshio intrusion onto the ECS shelf may take place year round, but seasonal Kuroshio intrusion occurs more often in winter than in summer. Only few intrusions occur during summer. A distinctive feature of the on-shelf intrusion is that both strong and weak intrusions (patterns 1 and 2) occur during winter-time, but the weak intrusion (pattern 2) dominates in early winter (September–November) and the strong intrusion (pattern 1) dominates in late winter (December–March). The findings about the seasonality of the Kuroshio intrusion presented in this study correspond well with various observations and model simu-

lations [e.g., Wu *et al.*, 2008; Ichikawa *et al.*, 2008; Hsin *et al.*, 2011]. For example, based on surface currents derived from HF radars, Ichikawa *et al.* [2008] demonstrated that the Kuroshio migration off northeast Taiwan is shoreward in winter and seaward in summer. Carrying out PCA of a high-resolution SST imagery, Hsin *et al.* [2011] also pointed out that the shoreward migration of the Kuroshio front frequently takes place in winter when the upstream Kuroshio transport off the eastern coast of Taiwan weakens.

What is the major forcing mechanism responsible for the seasonal Kuroshio variation off northeast Taiwan? Located along the pathway of the East Asian monsoon system, the circulation in the study region is largely influenced by the seasonal reversal of the monsoonal winds from northeasterly in winter to southwesterly in summer. Using a wind-driven model, Chao [1991] attributed the seasonal migration to the monsoonal winds. In winter (summer), onshore (offshore) Ekman transport by the northeasterly (southwesterly) monsoon forces the surface Kuroshio shoreward (seaward). On the other hand, a different mechanism was proposed by Oey *et al.* [2010] that the seasonal shift can be explained by SHF alone utilizing an idealized numerical model. Cooling produces downslope flux of dense shelf water that is compensated by shelfward

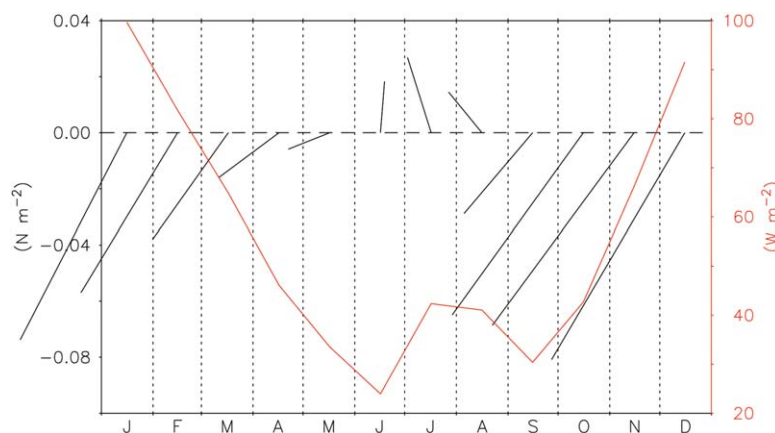


**Figure 8.** Climatology monthly stick plot of wind stress off north Taiwan superposed by zonal surface heat flux difference (SHFD) between two areas of 121°E–122.9°E, 24.8°N–26.7°N and 122.9°E–124.7°E, 24.8°N–26.7°N. Climatology monthly wind stress is obtained from the monthly CCMP wind field in 1993–2011. Climatological monthly SHFD is calculated from the NCEP reanalysis II heat flux data in 1993–2011.

intrusion. Parabolic isopycnals steepen eastward in winter and couple with the cross-shelf topographic slope (the Joint Effect of Baroclinicity and Relief (JEBAR) effect) to balance the enhanced intrusion [Oey *et al.*, 2010]. We then correlate percentages of BMUs of the four patterns with these two individual forces: the meridional wind stress and zonal SHF gradient. Here, the meridional wind stress is computed in the same domain as used in the GHSOM, while the zonal SHF difference between the two areas of 121°E–122.9°E, 24.8°N–26.7°N and 122.9°E–124.7°E, 24.8°N–26.7°N is calculated to stand for the SHF difference off north Taiwan.

The strong intrusion mode (pattern 1) is closely correlated with zonal SHF difference ( $\gamma = 0.87$ ), but a lower correlation exists between pattern 1 and the meridional wind stress in the vicinity ( $\gamma = -0.71$ ). The results confirm that the strong intrusion mode often occurs during wintertime from December to March of the following year and demonstrate that the zonal SHF gradient plays a major role in regulating the strong Kuroshio intrusion onto the shelf while the monsoon wind serves as the secondary factor. As Oey *et al.* [2010] proposed, the stronger JEBAR induced by stronger cooling enhances the on-shelf, cross-isobath intrusion in winter. On the other hand, the weak intrusion mode (pattern 2), which peaks primarily around the early winter (September–November), is more relevant to wind stress ( $\gamma = -0.64$ ), but not with zonal SHF difference ( $\gamma = 0.06$ ). As to another transitional pattern peaking in spring, pattern 3 shows an opposite outcome to pattern 2 that there is no correlation between pattern 3 and the wind stress ( $\gamma = 0.19$ ) but more and less related to the zonal SHF difference ( $\gamma = -0.55$ ). Pattern 4 shows significant seasonal variation, and is subject to summer monsoonal winds. The correlation coefficient between pattern 4 and the wind stress is 0.81. To sum up from the above analyses, winds via Ekman transport may influence the seasonal Kuroshio intrusion onto the ECS shelf all year round except spring whereas the zonal SHF gradient working as the JEBAR effect is more effective from the late winter (December) to the spring of the following year. In other words, when focusing on intrusion-prevailing seasons (winter and spring), the wind effect is dominant in the early winter while the surface heat flux gradient governs the intrusion in the rest period.

### 3.3. Interannual Variation of Wintertime Intrusion

As the BMU time series from 1993 to 2012 of the four patterns derived by the GHSOM shown in Figure 6, the interannual variations are evident in the four patterns. We focus on the Kuroshio intrusion patterns (patterns 1 and 2) because the on-shelf intrusion water provides a major source of nutrients to support primary production in the ECS. Both pattern 1 and pattern 2 prevail during the winter-like months, that is, the on-shelf intrusion in winter is a typical phenomenon. However, there are two exceptions shown in Figure 6, the winters of 1997–1998 and 2002–2003. Seldom intrusion events have been identified in these two winters. Even found, the intrusion events are shorter and have comparatively long nonintrusion events between them. To more quantitatively illustrate the interannual variation of the wintertime intrusion, Figure 9 depicts the percentages of BMUs of pattern 1, pattern 2, and sum of them averaged over the period from September to March of the following year. During the winters in 1993–2011, the occurrence of the intrusion mode peaks at the winters of 1998–1999, 2005–2006, 2009–2010, and 2010–2011 (sum > 80%), while it bottoms out in 1997–1998, and 2002–2003 (sum < 40%).

We used the KI index (defined in section 2.3; the green frame in Figure 5) to further investigate the interannual variability of the winter Kuroshio intrusion onto the ECS shelf. The southern boundary of this index roughly coincides with the 200 m isobath of the zonally running shelf break to indicate the on-shelf intrusion. To place emphasis on the interannual variability, the KI index is also averaged over the period from September to March of the following year. Figure 10 displays the time series of the KI index anomaly which reveals a significant year-to-year variation. Some discrepancy occurs between time series of the KI index and BMU of the GHSOM. With considering the magnitude of the KI index larger than one standard deviation (STD, about  $0.04 \text{ m s}^{-1}$ ), it reveals stronger intrusions in winters of 1998–1999 and 2010–2011 and weaker intrusion (or nonintrusion) in winters of 1997–1998 and 2002–2003. This nonintrusion feature during winters of 1997–1998 and 2002–2003 and its cause require a detailed examination.

As mentioned earlier, seasonal on-shelf intrusion fluctuations could be tracked back to the variation in the wind forcing, the zonal SHF gradient, or the upstream Kuroshio transport. Furthermore, local wind forcing contributes little for the interannual variability of the on-shelf intrusion ( $\gamma = -0.27$ ; figure not shown). On the other hand, the KI index shows a close correlation with zonal SHF difference ( $\gamma = 0.50$ ) and the upstream Kuroshio transport ( $\gamma = -0.56$ ). Thus, only the two factors are compared with the KI index. Figure 10 shows

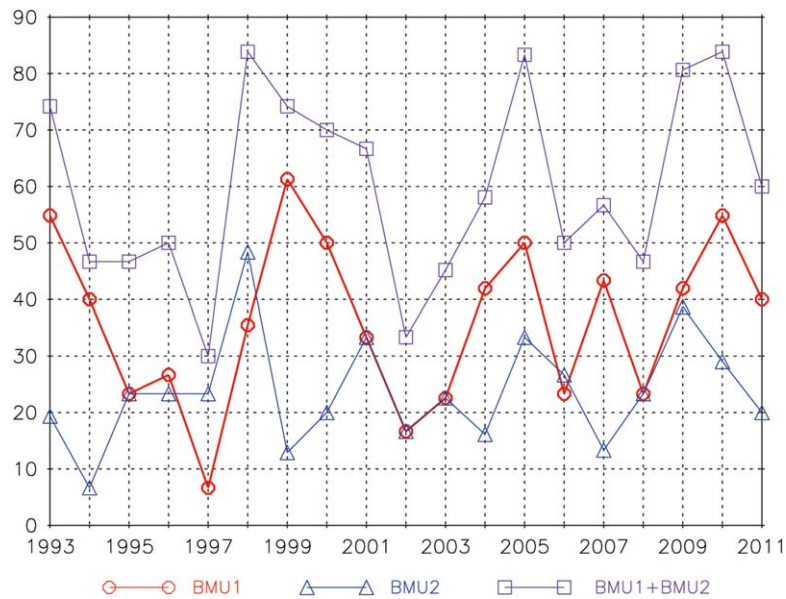


**Figure 9.** Percentages of BMUs of pattern 1 (red), pattern 2 (blue), and sum of them (purple) in the winters of 1993–2011. Percentage in a year for pattern1/pattern2/pattern1+2 is calculated by dividing the corresponding number by the sum of all patterns over a 7 month period from September to March of the following year.

anomalies of zonal SHF difference and the altimeter-derived Kuroshio transport off northeast Taiwan (the blue dashed section in Figure 1) alongside the KI indices during 1993–2011. Three significant negative values of zonal SHF difference anomaly peak during winters of 1997–1998, 2000–2001, and 2002–2003. Large and negative zonal SHF difference anomaly indicates less JEBAR effect and the eastward-flowing Kuroshio tends to follow the 200 m isobath, favoring the nonintrusion mode. However, these three winters with significant negative zonal SHF difference anomaly do not coincide with the two nonintrusion events in the winters of 1997–1998 and 2002–2003. The fluctuation of the upstream Kuroshio is responsible for this disagreement. As observed in radar-derived surface currents and SST imagery, the slower upstream Kuroshio velocity often accompanies northward movement of the Kuroshio axis and an on-shelf intrusion [Ichikawa *et al.*, 2008; Hsin *et al.*, 2011]. Figure 10 shows that the positive Kuroshio transport anomaly lasts from 1995 to 1997, following

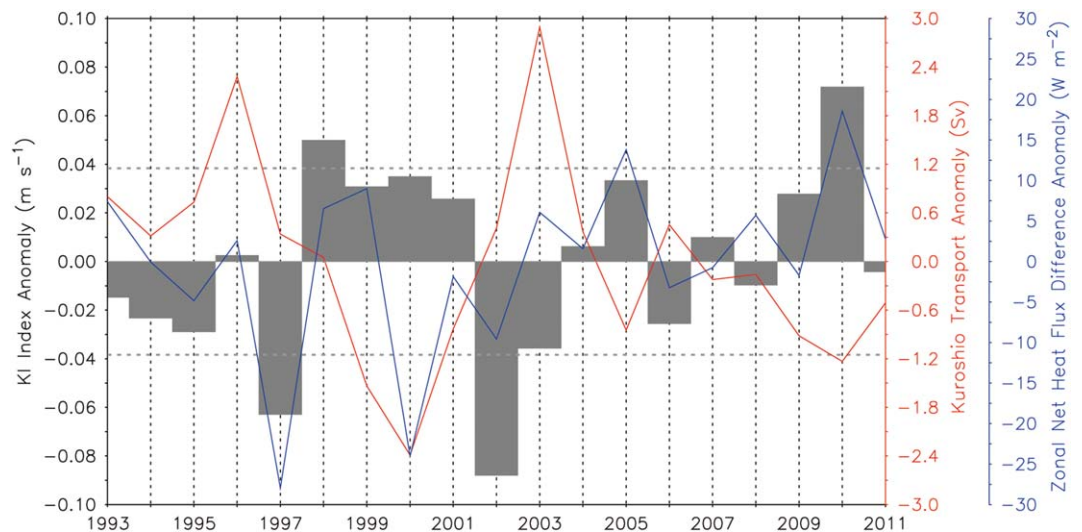


**Figure 10.** Time series of the KI index anomaly (gray, in  $m s^{-1}$ ), Kuroshio transport anomaly (red, in Sv), and zonal surface heat flux difference anomaly (blue, in  $W m^{-2}$ ) in winters of 1993–2011. All time series are obtained by averaging the original time series year to year over the period from September to March of the following year, with the removal of the mean. Horizontal gray dashed lines denote the  $\pm 1$  STD of the KI index anomaly.

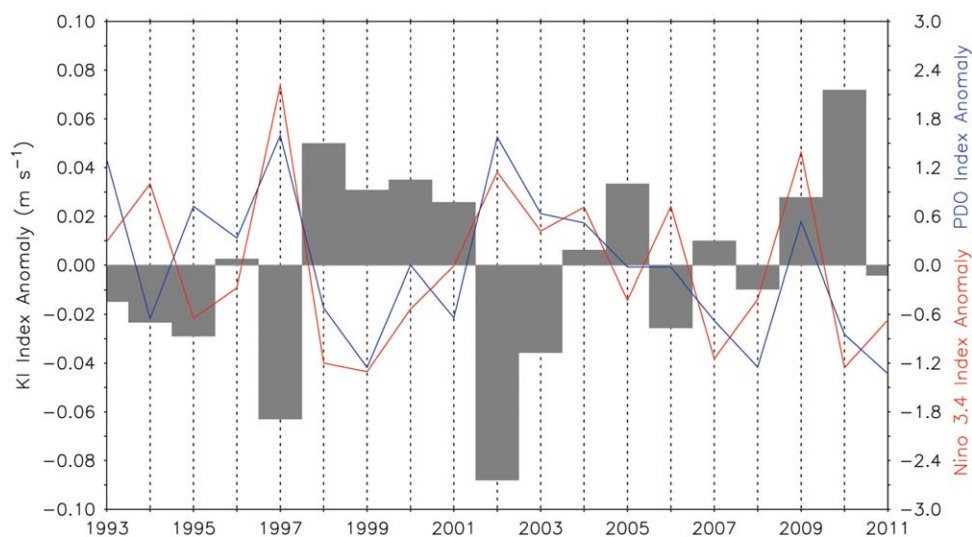


**Figure 11.** Same as Figure 10, but for the KI index anomaly (gray, in  $\text{m s}^{-1}$ ), Niño 3.4 index anomaly (red), PDO index anomaly (blue) in the winters of 1993–2011.

by a negative transport anomaly, with another large and positive anomaly in 2003. In the winter of 2000–2001, the significantly weakened Kuroshio induces the on-shelf intrusion regardless of the larger negative zonal SHF difference anomaly. On the other hand, in the winter of 1997–1998, the upstream Kuroshio transport anomaly is insignificant which indicates the Kuroshio is not weakened. The winter with large and negative zonal SHF difference anomaly implies negligible surface cooling near the coast of Taiwan. Accordingly, no cross-isobath intrusion is identified in the winter of 1997–1998. Similar scenario occurs in the winter of 2002–2003. The significant negative zonal SHF difference anomaly solely prevents the on-shelf intrusion.

Aside from the forcing mechanism driving the interannual variations of the Kuroshio intrusion onto the ECS shelf, one may also wonder whether the KI index is influenced by the well-known climate oscillation phenomena such as ENSO and PDO. To address this, the Niño 3.4 and PDO indices are superimposed in Figure 11. Similar to the KI index, both Niño 3.4 and PDO indices are averaged over the period from September to March of the following year. The KI index has a close relationship with both the Niño 3.4 index and the PDO index. The correlation between the KI index and the PDO index is significant at  $\gamma = -0.61$ , while that between the KI index and the Niño 3.4 index is also significant at  $\gamma = -0.66$ . The latter is consistent with findings in *Hwang and Kao* [2002]. Using TOPEX/POSEIDON altimeter data and a gravimetric geoid, *Hwang and Kao* [2002] derived 7 year time series of the Kuroshio transport off the northeastern coast of Taiwan, and related the volume transports to the ENSO index. They found that the Kuroshio transport variation off northeast Taiwan lags the ENSO index by 1 month with a correlation coefficient of 0.6. Interestingly, the two nonintrusion events take place only during the winters that both the Niño 3.4 index and the PDO index are large and positive (larger than one STD; Figure 11). Note that the opposite situation with large and negative values of both the Niño 3.4 and PDO indices cannot be adopted for explaining the intrusion events. The ENSO and the PDO may interplay and influence each other in some way, however it is not a target subject of this study.

#### 4. Conclusions

Satellite-derived geostrophic velocities correspond very well with various observations in the region. Seasonal fluctuations of the Kuroshio intensity and its zonal migration show up quite realistically in altimeter-based geostrophic velocities. The Kuroshio is weaker in winter, and the slower Kuroshio velocity often accompanies the on-shelf intrusion of the Kuroshio branch.

The GHSOM analysis of 20 year geostrophic velocity data reveals that the Kuroshio intrusion onto the ECS shelf occurs throughout the year. This study represents the possibility in overcoming the limitations of the observational data length, such as by drifters and moorings. The present study includes not only qualitative description but also quantitative analysis of Kuroshio intrusion patterns off northeast Taiwan. The results

provide a complete picture of the Kuroshio intrusion onto the shelf of the ECS. The on-shelf intrusion reveals both seasonal and interannual variations. On seasonal time scales the Kuroshio intrusion occurs more often in winter than in summer. Seldom intrusion events have been identified in summer. Both strong and weak intrusions occur during wintertime, but the weak intrusion prevails in early winter and the strong intrusion predominates in late winter. Different forcing mechanisms are responsible for the strong and weak intrusions. The strong on-shelf intrusion is closely correlated with both zonal SHF gradient and wind stress while the weak intrusion is only related to wind stress in the vicinity.

Beyond a seasonal time scale, the winter Kuroshio intrusion demonstrates an interannual variation that is related to the ENSO and the PDO. Although on-shelf intrusion is the major characteristic of the region during wintertime, seldom intrusion events have been identified in the winters of 1997–1998 and 2002–2003. These two nonintrusion events take place during the winters when both the Niño 3.4 index and the PDO index are large and positive. Local wind forcing contributes little for the interannual variability of the intrusion, while the combination of the SHF gradient and upstream Kuroshio intensity modulates the on-shelf intrusion pattern. In the winters of 1997–1998 and 2002–2003, the Kuroshio transport anomaly is insignificant and there is no winter cooling because zonal SHF difference anomaly is large and negative. The shelf water is relatively warm and on-shelf intrusion ceases. No JEBAR effect has been generated by cooling and the Kuroshio tends to follow the 200 m isobath, favoring the nonintrusion mode. On the other hand, in the winter of 2000–2001, the significantly weakened Kuroshio induces the on-shelf intrusion regardless of negative zonal SHF difference. This interannual changes of the Kuroshio intensity in the upstream area east of Taiwan is ascribed to the relative intensity of cyclonic eddies to anticyclonic eddies originated in the Pacific STCC area.

#### Acknowledgments

This research was supported by the Ministry of Science and Technology, Taiwan, ROC, under grants MOST 101–2611-M-003-002-MY3, 102–2611-M-001-001-MY2, and 102–2811-M-003–020. The AVISO altimeter products were produced by Ssalto/Duacs and distributed by Aviso, with support from Cnes.

#### References

- Chang, Y.-L., and L.-Y. Oey (2011), Interannual and seasonal variations of Kuroshio transport east of Taiwan inferred from 29 years of tide-gauge data, *Geophys. Res. Lett.*, *38*, L08603, doi:10.1029/2011GL047062.
- Chao, S.-Y. (1991), Circulation of the East China Sea, a numerical study, *J. Oceanogr. Soc. Jpn.*, *42*(6), 273–295, doi:10.1007/BF02123503.
- Chen, C.-T. A. (1996), The Kuroshio intermediate water is the major source of nutrients on the East China Sea continental shelf, *Oceanol. Acta*, *19*(5), 523–527.
- Hsin, Y.-C., C.-R. Wu, and P.-T. Shaw (2008), Spatial and temporal variations of the Kuroshio east of Taiwan, 1982–2005: A numerical study, *J. Geophys. Res.*, *113*, C04002, doi:10.1029/2007JC004485.
- Hsin, Y.-C., T. Qu, and C.-R. Wu (2010), Intra-seasonal variation of the Kuroshio southeast of Taiwan and its possible forcing mechanism, *Ocean Dyn.*, *60*, 1293–1306, doi:10.1007/s10236-010-0294-2.
- Hsin Y.-C., T.-L. Chiang, and C.-R. Wu (2011), Fluctuations of the thermal fronts off northeastern Taiwan, *J. Geophys. Res.*, *116*, C10005, doi:10.1029/2011JC007066.
- Hsin, Y.-C., B. Qiu, T.-L. Chiang, and C.-R. Wu (2013), Seasonal to interannual variations in the intensity and central position of the surface Kuroshio east of Taiwan, *J. Geophys. Res. Oceans*, *118*, 4305–4316, doi:10.1002/jgrc.20323.
- Hwang, C., and R. Kao (2002), TOPEX/POSEIDON-derived space-time variations of the Kuroshio Current: Applications of a gravimetric geoid and wavelet analysis, *Geophys. J. Int.*, *151*(3), 835–847, doi:10.1046/j.1365-246X.2002.01811.x.
- Hwang, C., C.-R. Wu, and R. Kao (2004), TOPEX/Poseidon observations of mesoscale eddies over the Subtropical Countercurrent: Kinematic characteristics of an anticyclonic eddy and a cyclonic eddy, *J. Geophys. Res.*, *109*, C08013, doi:10.1029/2003JC002026.
- Ichikawa, K., R. Tokeshi, M. Kashima, K. Sato, T. Matsuoka, S. Kojima, and S. Fujii (2008), Kuroshio variations in the upstream region as seen by HF radar and satellite altimetry data, *Int. J. Remote Sens.*, *29*(21), 6417–6426, doi:10.1080/01431160802175454.
- Johns, W. E., T. N. Lee, D. Zhang, R. Zantopp, C.-T. Liu, and Y. Yang (2001), The Kuroshio east of Taiwan: Moored transport observations from the WOCE PCM-1 array, *J. Phys. Oceanogr.*, *31*(4), 1031–1053, doi:10.1175/1520-0485(2001)031<1031:TKEOTM>2.0.CO;2.
- Kohonen, T. (2001), *Self-Organizing Maps*, *Inf. Sci. Ser.*, vol. 30, 3rd ed., Springer, Berlin.
- Liang, W.-D., T. Y. Tang, Y.-J. Yang, M.-T. Ko, and W.-S. Chuang (2003), Upper-ocean currents around Taiwan, *Deep Sea Res., Part II*, *50*(6–7), 1085–1105, doi:10.1016/S0967-0645(03)00011-0.
- Lie, H.-J., and C.-H. Cho (2002), Recent advances in understanding the circulation and hydrography of the East China Sea, *Fish. Oceanogr.*, *11*(6), 318–328, doi:10.1046/j.1365-2419.2002.00215.x.
- Liu, Y., and R. H. Weisberg (2005), Patterns of ocean current variability on the West Florida Shelf using the self-organizing map, *J. Geophys. Res.*, *110*, C06003, doi:10.1029/2004JC002786.
- Liu, Y., R. H. Weisberg, and R. He (2006), Sea surface temperature patterns on the west Florida Shelf using Growing Hierarchical Self-Organizing Maps, *J. Atmos. Oceanic Technol.*, *23*(2), 325–338, doi:10.1175/JTECH1848.1.
- Oey, L.-Y., Y.-C. Hsin, and C.-R. Wu (2010), Why does the Kuroshio northeast of Taiwan shift shelfward in winter?, *Ocean Dyn.*, *60*(2), 413–426, doi:10.1007/s10236-009-0259-5.
- Rio, M. H., S. Guinehut, and G. Larnicol (2011), New CNES-CLS09 global mean dynamic topography computed from the combination of GRACE data, altimetry, and in situ measurements, *J. Geophys. Res.*, *116*, C07018, doi:10.1029/2010JC006505.
- Sun, X. (1987), Analysis of the surface path of the Kuroshio in the East China Sea, in *Essays on Investigation of Kuroshio*, edited by X. Sun, pp. 1–14, China Ocean Press, Beijing, China.
- Tsui, I.-F., and C.-R. Wu (2012), Variability analysis of Kuroshio intrusion through Luzon Strait using growing hierarchical self-organizing map, *Ocean Dyn.*, *62*(8), 1187–1194, doi:10.1007/s10236-012-0558-0.
- Wu, C.-R. (2013), Interannual modulation of the Pacific Decadal Oscillation (PDO) on the low-latitude western North Pacific, *Prog. Oceanogr.*, *110*, 49–58, doi:10.1016/j.pocean.2012.12.001.
- Wu, C.-R., H.-F. Lu, and S.-Y. Chao (2008), A numerical study on the formation of upwelling off northeast Taiwan, *J. Geophys. Res.*, *113*, C08025, doi:10.1029/2007JC004697.
- Yang, Y., C.-T. Liu, T. N. Lee, W. Johns, H.-W. Li, and M. Koga (2001), Sea surface slope as an estimator the Kuroshio volume transport east of Taiwan, *Geophys. Res. Lett.*, *28*(12), 2461–2464, doi:10.1029/2000GL011709.